Ultrafast strong-field photoelectron emission due to two-color laser fields

Yi Luo and Peng Zhang*

Department of Electrical and Computer Engineering, Michigan State University, East Lansing, Michigan 48824-1226, USA

(Received 2 August 2018; revised manuscript received 11 October 2018; published 29 October 2018)

Electron emission from solids driven by two-color lasers provides great flexibility for the control of electron dynamics in ultrashort spatiotemporal scales due to the interference effect. Here, we construct an analytical model for the highly nonlinear photoelectron emission from a metal surface illuminated by two-color laser fields, by solving the time-dependent Schrödinger equation. The exact solution is valid for arbitrary harmonic orders, laser intensities, phase difference between two lasers, and metal work function and Fermi level. We find two-color lasers can strongly modulate both the electron energy spectra and the emission current up to 99%. Using the same input parameters, our theoretical prediction for the photoemission current modulation depth (93.9%) is almost identical to the experimental result (94%) in [M. Förster *et al.*, Phys. Rev. Lett. **117**, 217601 (2016)].

DOI: 10.1103/PhysRevB.98.165442

I. INTRODUCTION

Laser-induced electron emission from solids [1–8] offers a platform to coherently control electron dynamics in ultrashort spatiotemporal scales [9–13]. It is fundamentally important to the advancement of ultrafast electron microscopes [14,15], tabletop particle accelerators and x-ray sources [16], and future quantum nanocircuits [17–19]. The mechanisms of electron emission driven by a single-frequency laser have been extensively studied both theoretically [20–24] and experimentally [1–3,25,26], including transition from multiphoton absorption to optical field emission [2], electron emission energy distribution [3], effects of carrier-envelope phase [25], local nonuniform fields [4], dc bias [1,24], and short pulse excitation [11]. Recently, two-color photoemission from nanotips driven by a fundamental and a weak second-harmonic laser pulse has been demonstrated experimentally [27,28], showing substantial emission current modulation. However, the underlying physics for the correlation between two-color laser fields and various electron emission processes is not well understood. The parametric dependence of the electron emission properties requires substantial further study.

Here, we present an analytical model for ultrafast electron emission from a metal surface driven by two-color lasers. By solving the time-dependent Schrödinger equation exactly, our solution is applicable for arbitrary fundamental and harmonic laser frequencies, laser intensities, phase delays, cathode work function and Fermi level. Various emission mechanisms such as multiphoton absorption, photon-induced over-barrier emission, strong optical field emission, and various combinations of them are all captured in a single formulation. We identify the condition for the maximum emission current modulation by superimposing a weak harmonic laser on a fundamental laser, showing excellent agreement with the experimental observation [27]. This work provides clear insights to control both the photoelectron energy distribution and the current modulation depth using two-color lasers.

II. EXACT FORMULATION

Our one-dimensional (1D) model (Fig. 1) assumes electrons with initial energy ε are emitted from the metal-vacuum interface at $x = 0$ under the illumination of two-color laser fields, $F_1\cos(\omega t)$ and $F_2\cos(\beta\omega t + \theta)$, where F_1 and F_2 are the magnitudes of the laser fields, ω is the fundamental laser frequency, β is a positive integer, and θ is the relative phase. We assume both laser fields are perpendicular to the metal surface, and cut off abruptly at the surface [24]. The sudden screening of external fields may be justified, because the laser penetration depth (i.e., skin depth) is typically much smaller than the laser wavelength (e.g., for the gold, the skin depth of an 800-nm laser wavelength is around 4 nm) [24]. For simplicity, the scattering effects of photoexcited electrons with phonons and other electrons, which may happen in the penetration depth, are also ignored in our model. A time-varying potential barrier would be created by the two laser fields at the metal-vacuum interface $x = 0$,

$$\Phi(x,\ t) = \begin{cases} 0, & x < 0 \\ V_0 - eF_1 x\cos(\omega t) - eF_2 x\cos(\beta\omega t + \theta), & x \geqslant 0, \end{cases} \tag{1}$$

where $V_0 = E_F + W$; E_F and W are the Fermi energy and work function of the metal, respectively; and e is the elementary charge. To make the analytical treatment feasible, image charge effects [29] are not included in Eq. (1). However, our previous work [24] demonstrated a very good approximation to include the image charge potential in our model, by simply replacing the work function W with the effective work function due to Schottky barrier lowering.

The electron wave function $\psi(x,\ t)$ is solved from the time-dependent Schrödinger equation,

$$i\hbar\frac{\partial\psi(x,\ t)}{\partial t} = -\frac{\hbar^2}{2m}\frac{\partial^2\psi(x,\ t)}{\partial x^2} + \Phi(x,\ t)\psi(x,\ t), \tag{2}$$

where $\hbar$ is the reduced Plank constant, m is the electron mass, and $\Phi(x,\ t)$ is the potential energy given in Eq. (1).

*Corresponding author: pz@egr.msu.edu

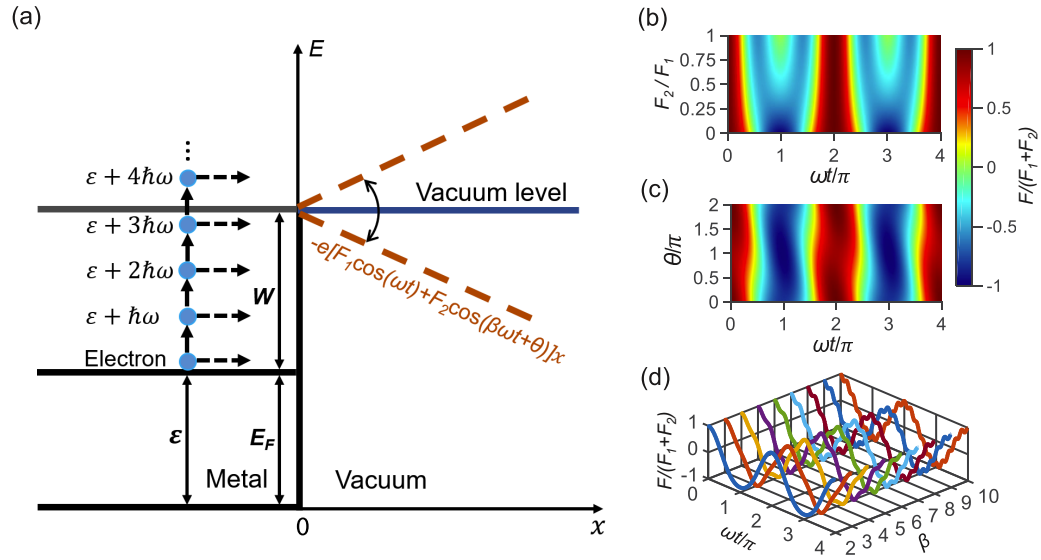

FIG. 1. Photoemission under illumination of two-color laser fields. (a) Energy diagram for electron emission through a wiggling potential barrier induced by two-color laser fields across the metal-vacuum interface at $x = 0$. Electrons with initial energy of ε are excited to emit through n-photon absorption, with a transmitted energy of $\varepsilon + n\hbar\omega$, with n being an integer. The fundamental and the harmonic laser fields are $F_1\cos(\omega t)$ and $F_2\cos(\beta\omega t + \theta)$, respectively. E_F and W are the Fermi energy and work function of the metal, respectively. Strong interference is shown in the time-dependent total laser field $F = F_1\cos(\omega t) + F_2\cos(\beta\omega t + \theta)$ as a function of (b), relative laser fields strength F_2/F_1, with $\beta = 2$ and $\theta = 0$; (c) relative phase difference θ, with $F_2/F_1 = 0.1$ and $\beta = 2$; and (d) harmonic order β, with $F_2/F_1 = 0.1$ and $\theta = 0$.

An exact solution to Eq. (2) for $x \geqslant 0$ is obtained (see Appendix for more details),

$$\psi(x,\ t) = \sum_{n=-\infty}^{\infty} T_n \exp\left(-i\varepsilon t/\hbar - in\omega t\right) \exp\left(i\xi\sqrt{2mE_n/\hbar^2}\right) \times \exp\left(\frac{ie}{\hbar}Lx + \frac{ie^2}{8\hbar m}M - \frac{ie^2F_1F_2}{2\beta\hbar m\omega^2}N\right), \quad x \geqslant 0, \tag{3}$$

where $\xi = x + \frac{eF_1\cos(\omega t)}{m\omega^2} + \frac{eF_2\cos(\beta\omega t+\theta)}{m\beta^2\omega^2}$, $L = \frac{F_1\sin(\omega t)}{\omega} + \frac{F_2\sin(\beta\omega t+\theta)}{\beta\omega}$, $M = \frac{F_1^2\sin(2\omega t)}{\omega^3} + \frac{F_2^2\sin(2\beta\omega t+2\theta)}{\beta^3\omega^3}$, $N = \frac{\sin[(\beta-1)\omega t+\theta]}{(\beta-1)\omega} - \frac{\sin[(\beta+1)\omega t+\theta]}{(\beta+1)\omega}$, T_n is the transmission coefficient, the drift kinetic energy $E_n = \varepsilon + n\hbar\omega - E_F - W - U_{p1} - U_{p2}$, the ponderomotive energies $U_{p1} = e^2F_1^2/4m\omega^2$, and $U_{p2} = e^2F_2^2/4m\beta^2\omega^2$, and ε is the electron initial energy. Because of the time periodicity, Eq. (3) represents the superposition of transmitted electron plane waves with energies $\varepsilon + n\hbar\omega$, due to multiphoton absorption ($n > 0$), tunneling ($n = 0$), and multiphoton emission ($n < 0$) [21,24].

For $x < 0$, the solution to Eq. (2) is

$$\psi(x,\ t) = \exp\left(-\frac{i\varepsilon t}{\hbar} + ik_0x\right) + \sum_{n=-\infty}^{\infty} R_n \exp\left(-i\frac{\varepsilon + n\hbar\omega}{\hbar}t - ik_nx\right), \quad x < 0, \tag{4}$$

which denotes the superposition of an incident wave and a set of reflected waves, where $k_0 = \sqrt{2m\varepsilon/\hbar^2}$, $k_n = \sqrt{2m(\varepsilon + n\hbar\omega)/\hbar^2}$, and R_n is the reflection coefficient. It has been verified that most of the reflected current is through the initial energy level ($n = 0$) [24].

By matching the solutions in Eqs. (3) and (4) from the conditions that both $\psi(x,\ t)$ and $\partial\psi(x,\ t)/\partial x$ are continuous at $x = 0$, and taking the Fourier transform, we obtain, in nondimensional quantities [24], $\bar{\varepsilon} = \varepsilon/W$, $\bar{\omega} = \omega\hbar/W$, $\bar{t} = tW/\hbar$, $\bar{E}_F = E_F/W$, $\bar{x} = x/\lambda_0$, $\lambda_0 = \sqrt{\hbar^2/2mW}$, $\bar{F}_1 = F_1e\lambda_0/W$, $\bar{F}_2 = F_2e\lambda_0/W$, $\bar{U}_{p1} = U_{p1}/W$, $\bar{U}_{p2} = U_{p2}/W$, the following equation,

$$2\sqrt{\bar{\varepsilon}}\delta(l) = \sum_{n=-\infty}^{\infty} T_n[\sqrt{\bar{\varepsilon} + l\bar{\omega}}P_{n(n-l)} + Q_{n(n-l)}], \tag{5}$$

where $\delta(l)$ is the Dirac delta function, and $P_{n(n-l)}$, and $Q_{n(n-l)}$ are given by

$$P_{nl} = \frac{1}{2\pi}\int_0^{2\pi} p_n(\bar{\omega}\bar{t})e^{-il\bar{\omega}\bar{t}}d(\bar{\omega}\bar{t}),$$

$$Q_{nl} = \frac{1}{2\pi}\int_0^{2\pi} p_n(\bar{\omega}\bar{t})z_n(\bar{\omega}\bar{t})e^{-il\bar{\omega}\bar{t}}d(\bar{\omega}\bar{t}), \tag{6a}$$

$$p_n(\bar{\omega}\bar{t}) = q(\bar{\omega}\bar{t})f(\bar{\omega}\bar{t}),$$

$$z_n(\bar{\omega}\bar{t}) = \sqrt{\bar{E}_n} + \frac{\bar{F}_1}{\bar{\omega}}\sin(\bar{\omega}\bar{t}) + \frac{\bar{F}_2}{\beta\bar{\omega}}\sin(\beta\bar{\omega}\bar{t} + \theta), \tag{6b}$$

$$q(\bar{\omega}\bar{t}) = e^{i2\sqrt{\bar{E}_n}[\frac{\bar{F}_1\cos(\bar{\omega}\bar{t})}{\bar{\omega}^2} + \frac{\bar{F}_2\cos(\beta\bar{\omega}\bar{t}+\theta)}{\beta^2\bar{\omega}^2}]}, \tag{6c}$$

$$f(\bar{\omega}\bar{t}) = e^{i[\frac{\bar{F}_1^2\sin(2\bar{\omega}\bar{t})}{4\bar{\omega}^3} + \frac{\bar{F}_2^2\sin(2\beta\bar{\omega}\bar{t}+2\theta)}{4\beta^3\bar{\omega}^3}]}e^{-\frac{i\bar{F}_1\bar{F}_2}{\beta\bar{\omega}^2}\{\frac{\sin[(\beta-1)\bar{\omega}\bar{t}+\theta]}{(\beta-1)\bar{\omega}} - \frac{\sin[(\beta+1)\bar{\omega}\bar{t}+\theta]}{(\beta+1)\bar{\omega}}\}}, \tag{6d}$$

with $\bar{E}_n = \bar{\varepsilon} + n\bar{\omega} - \bar{E}_F - \bar{U}_{p1} - \bar{U}_{p2} - 1$. In Eq. (6b), p_n and z_n denote the phase factor of the wave function in the nth state and of its spatial derivative at $\bar{x} = 0$, respectively. P_{nl} and Q_{nl} are the lth Fourier coefficients

of p_n and the product of p_n and z_n, respectively. The transmission coefficient T_n (and therefore the reflection coefficient R_n) is obtained from Eq. (5). The emission current density is then calculated from the probability current density $J(x,\ t) = (i\hbar/2m)(\psi\partial\psi^*/\partial x - \psi^*\partial\psi/\partial x) = (i\hbar/2m)\sum_{n=-\infty}^{\infty}\sum_{l=-\infty}^{\infty}(\psi_n\partial\psi_l^*/\partial x - \psi_n^*\partial\psi_l/\partial x)$, where $\psi(x,t) = \sum_{n=-\infty}^{\infty}\psi_n(x,t)$ is obtained from Eq. (3).

The normalized emission current density, defined as the ratio of the transmitted probability current density over the incident probability current density, $w(\varepsilon,\ x,\ t) = J_t(\varepsilon,\ x,\ t)/J_i(\varepsilon,\ x,\ t)$, is found in nondimensional form as

$$w(\bar{\varepsilon},\ \bar{x},\ \bar{t}) = \frac{1}{\sqrt{\bar{\varepsilon}}}\sum_{n=-\infty}^{\infty}\sum_{l=-\infty}^{\infty}\mathrm{Re}[e^{i(l-n)\bar{\omega}\bar{t}}T_nT_l^*e^{i\Theta}D], \quad (7)$$

where $\Theta = [\sqrt{\bar{E}_n} - (\sqrt{\bar{E}_l})^*][\bar{x} + \frac{2\bar{F}_1}{\bar{\omega}^2}\cos(\bar{\omega}\bar{t}) + \frac{2\bar{F}_2}{\beta^2\bar{\omega}^2}\cos(\beta\bar{\omega}\bar{t} + \theta)]$, and $D = (\sqrt{\bar{E}_l})^* + \frac{\bar{F}_1}{\bar{\omega}}\sin(\bar{\omega}\bar{t}) + \frac{\bar{F}_2}{\beta\bar{\omega}}\sin(\beta\bar{\omega}\bar{t} + \theta)$. The normalized time-averaged emission current density is found to be

$$\langle w(\bar{\varepsilon})\rangle = \sum_{n=-\infty}^{\infty}\langle w_n(\bar{\varepsilon})\rangle, \quad \langle w_n(\bar{\varepsilon})\rangle = \mathrm{Re}(|T_n|^2\sqrt{\bar{E}_n/\bar{\varepsilon}}), \quad (8)$$

where $\langle w_n\rangle$ represents the emission current density through the nth channel, with emitted electrons of energy $\varepsilon + n\hbar\omega$ due to the n-photon contribution. Since most of the electrons emitted from sources are located near the Fermi level [21,24,30,31], we take the initial electron energy $\varepsilon = E_F$ for the calculations in this paper.

III. RESULTS AND DISCUSSION

Figure 2 shows the photoelectron energy spectra, under different two-color laser fields F_1 (at frequency ω) and F_2 (at second harmonic 2ω), for various phase differences θ between two laser fields, calculated from Eq. (8). The wavelength of the fundamental laser is 800 nm ($\hbar\omega = 1.55$ eV). The metal is assumed to be gold [2,21,31], with Fermi energy $E_F = 5.53$ eV and the work function $W = 5.1$ eV. Unless mentioned otherwise, these are the default values for the calculations in this paper. The dominant emission process is the four-photon absorption ($n = 4$) for the fundamental laser (or two-photon absorption for the second-harmonic laser), where electrons at the Fermi level need to absorb at least four photons to overcome the potential barrier ($W/\hbar\omega = 3.29$) (cf. Fig. 1). For $n < 4$, the emission probability is identically zero. When the two laser fields are in phase ($\theta = 0$), the photoelectron emission spectrum becomes broader and the total emission current density $\langle w\rangle = \sum_n\langle w_n\rangle$ increases when either F_1 or F_2 increases, since more channels open up for electron emission. When F_1 is small [see Fig. 2(a)], the emission spectrum is very close to that driven by the second-harmonic laser F_2 alone, indicating F_2 dominates the emission process. As F_1 increases [from Fig. 2(a) to Fig. 2(e)], the emission spectrum gradually transits to that driven by F_1 alone, indicating the laser field dominating the emission process changes from F_2 to F_1. During the transition process, the competition between F_1 and F_2 for dominating the electron emission causes the dip in Fig. 2(c). In Figs. 2(d) and 2(e), the dip shifts to larger n as F_1 increases, due to the channel closing effect [21,24]. When either $F_1 = 0$ or $F_2 = 0$, the results recover those of single-frequency laser-induced photoemission [21,24]. Figures 2(f)–2(j) show that

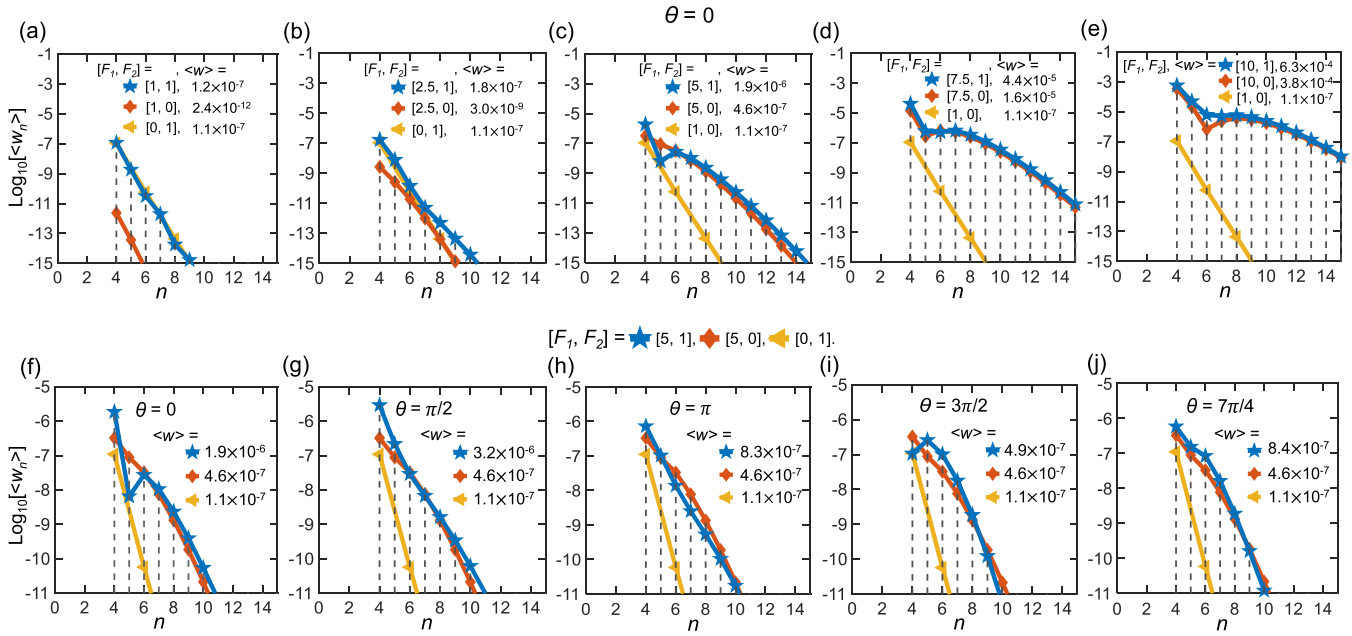

FIG. 2. Photoelectron energy spectra, calculated from Eq. (8). (a)–(e) Energy spectra under different combinations of two-color laser fields F_1 (at frequency ω) and F_2 (at frequency 2ω), for the special case of $\theta = 0$. (f)–(j) Energy spectra for various phase differences θ, for $[F_1, F_2] = [5,\ 1]$, $[5,\ 0]$, and $[0,\ 1]$ V/nm. A clear modulation in both the energy spectrum and the total emission current $\langle w\rangle$ is observed, due to the interference effect between the two-color lasers. The unit of laser fields F_1 and F_2 is V/nm in all figures.

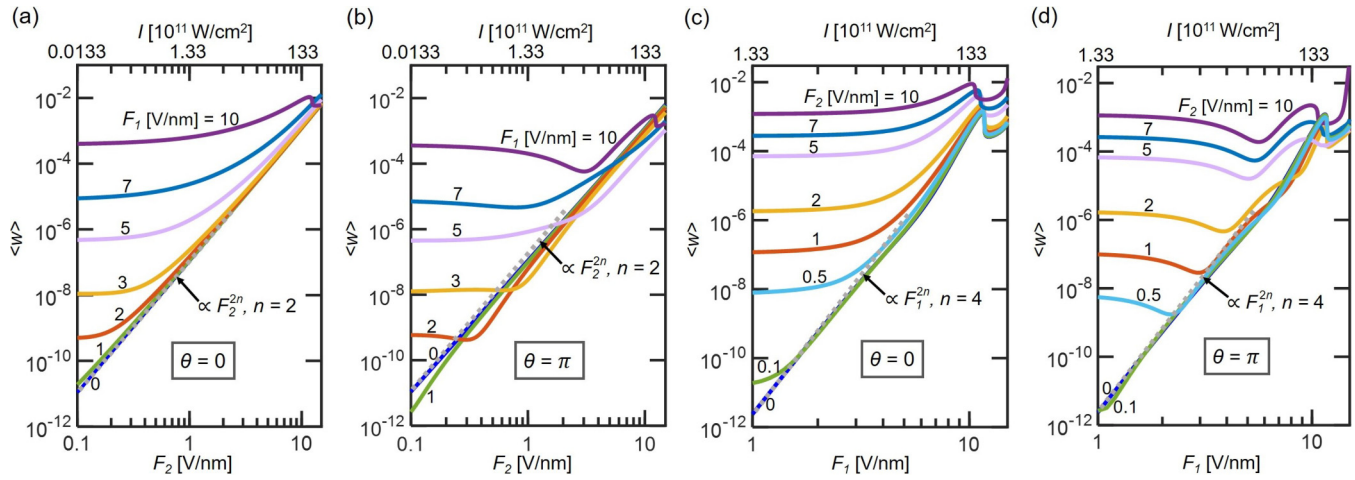

FIG. 3. Normalized total time-averaged emission current density for the phase differences $\theta = 0$ and π. (a), (b) Total time-averaged current density $\langle w \rangle$ as a function of the second-harmonic laser field F_2, under various fundamental laser fields F_1. (c), (d) $\langle w \rangle$ as a function of F_1, under various F_2. The laser intensity is related to the laser electric field as $I(\mathrm{W/cm^2}) = 1.33 \times 10^{11}\,[F_1(\mathrm{V/nm})]^2$. The dotted lines represent the scale $\langle w \rangle \propto F^{2n}$.

the emission spectra can be greatly modified as θ changes, due to the interference effect between the two lasers. For example, when θ changes from $\pi/2$ to $3\pi/2$, the emission process with the highest probability shifts from the four-photon ($n = 4$) to five-photon ($n = 5$) absorption.

Figure 3 shows the normalized total time-averaged emission current density $\langle w \rangle$ under various combinations of F_1 and F_2, for the phase differences $\theta = 0$ and π. In Figs. 3(a) and 3(b), when F_2 is small ($F_1/F_2 > 10$), $\langle w \rangle$ is insensitive to F_2, because the fundamental laser F_1 dominates the emission process. As F_2 increases, the current density gradually approaches the scale $\langle w \rangle \propto F_2^{2n}$ with $n = 2$ [see Figs. 3(a) and 3(b)], indicating two-photon absorption (or four-photon with respect to the fundamental laser of $\hbar\omega$) is the main emission process. The gradual change of the slope of $\langle w \rangle$ is due to the opening up of higher emission channels, as seen in Fig. 2. When $\theta = \pi$ [see Fig. 3(b)], a series of new dips appears in the curves as compared to those when $\theta = 0$

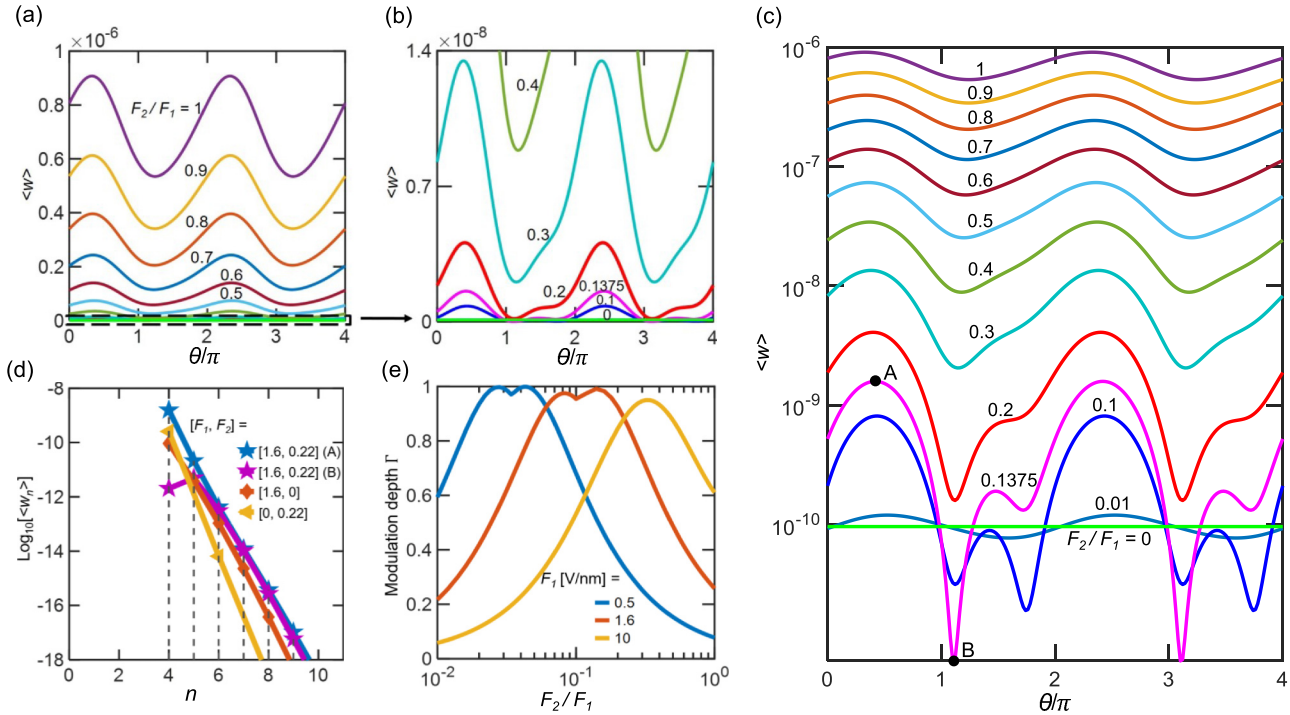

FIG. 4. Current modulation depth. (a) Normalized total time-averaged emission current density $\langle w \rangle$ as a function of the phase difference θ, under different F_2/F_1. (b) Magnification of the bottom area of (a). (c) Semilog plot of $\langle w \rangle$ in (a). F_1 is fixed at 1.6 V/nm in (a)–(c). (d) Electron energy spectra of $\langle w \rangle_{\max}$ (point A) and $\langle w \rangle_{\min}$ (point B) for $F_2/F_1 = 0.1375$ in (c). (e) Current modulation depth Γ as a function of the field ratio F_2/F_1 for different $F_1 = 0.5,\ 1.6,\ 10\,\mathrm{V/nm}$.

[see Fig. 3(a)], indicating strong interference effects between the two lasers. The interference effect is also reflected in that the total current density $\langle w \rangle$ with $F_1 = 1$ V/nm changes from being larger than $\langle w \rangle$ with $F_1 = 0$ (i.e., by F_2 only) to being smaller [see the green and dark blue lines in Figs. 3(a) and 3(b)]. The sharp drops of $\langle w \rangle$ at $F_2 = 13$ V/nm in Figs. 3(a) and 3(b) are due to the channel closing effect [21,24], which is accurately predicted by taking $E_4 = \varepsilon + 4\hbar\omega - E_F - W - U_{p1} - U_{p2} = 0$, giving $F_2 = 12.4$ V/nm. Similar behaviors of $\langle w \rangle$ as a function of F_1 are observed in Figs. 3(c) and 3(d).

The total time-averaged emission current density $\langle w \rangle$ as a function of θ is shown in Figs. 4(a)–4(c), for various 2ω laser field F_2 with fixed $F_1 = 1.6$ V/nm. The total emission current density $\langle w \rangle$ oscillates as a sinusoidal function of θ, showing striking resemblance to the experimentally measured emission current (see Fig. 2(b) in Ref. [27]). As F_2 decreases, the maximum and minimum of $\langle w \rangle$ both decrease, but the corresponding θ for the maximum and minimum $\langle w \rangle$ remain almost unchanged. The modulation depth, defined as $\Gamma = (\langle w \rangle_{\max} - \langle w \rangle_{\min})/(\langle w \rangle_{\max} + \langle w \rangle_{\min})$, reaches a maximum value of approximately 99% when $F_2/F_1 = 0.1375$ (or intensity ratio of 2%). For tungsten and the fundamental laser wavelength of 1560 nm (not shown in Fig. 4) as in Ref. [27], we obtain the modulation depth of 95.5% and of 93.9%, when setting the work function in Eq. (1) to be 4.3 eV and 3.6 eV (effective work function with Schottky effect), respectively. The latter is almost identical to the experimentally measured modulation depth of 94% in Ref. [27]. Despite the excellent agreement between the theoretical predictions and the experiments, we should stress that our model assumed a one-dimensional flat metal surface, whereas the experiment used a nanometer scale sharp emitter [27]. The sharpness of the emitter may introduce varying field enhancement and the Schottky lowering factor along the emission surface, nonuniform off-tip electron emission [32], and even quantized energy levels inside the emitter [33]. In addition, our model neglects the image charge potential, laser pulse shape, laser penetration depth, incident electron energy distribution inside the metal, and surface effects (e.g., local surface roughness, grain boundaries, and different crystal plane terminations). As F_2 further decreases, Γ drops. When F_2 reaches 0, $\langle w \rangle$ becomes a constant, with zero Γ as expected, as shown in Fig. 4(c). Figure 4(d) compares the electron energy spectra at the peak and valley of the current modulation for $F_2/F_1 = 0.1375$, where the dominant emission process shifts from four-photon to five-photon absorption. Figure 4(e) summarizes the modulation depth Γ as a function of F_2/F_1, for different strengths of the fundamental ω laser field F_1. As the ω laser field F_1 increases, the location of the peak modulation depth shifts to larger F_2/F_1, since a larger 2ω laser field F_2 is needed to balance the increase of F_1 for achieving the same modulation depth.

Figure 5 shows the time-dependent electron emission current density $w(\bar{x}, t)$ as a function of the space $\bar{x}$ and time t, for ω laser field $F_1 = 1.6$ V/nm and 2ω laser field $F_2 = 0.22$ V/nm. When $\bar{x}$ is greater than 20 (beyond the strong surface current oscillation region), the emission current keeps the same temporal profile with only a phase shift as $\bar{x}$ increases [see Figs. 5(a) and 5(b)], which is primarily due to the drift and acceleration motion of electrons under the influence

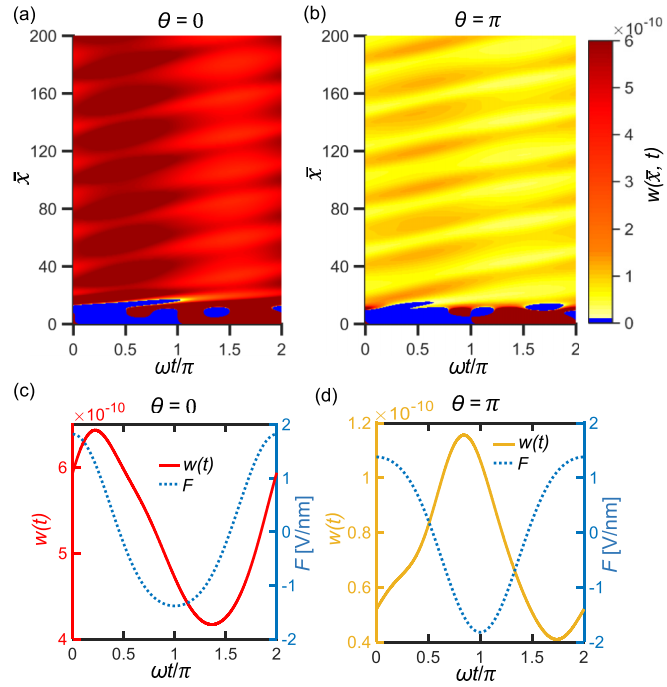

FIG. 5. Total time-dependent emission current density for the phase differences $\theta = 0$ and π. (a), (b) Total time-dependent emission current density $w(\bar{x}, t)$ as a function of the space $\bar{x}$ and time t. (c), (d) Total emission current density $w(t)$ at $\bar{x} = 100$ as a function of time t. Dotted lines in (c), (d) are for the total time-dependent laser field $F = F_1\cos(\omega t) + F_2\cos(\beta\omega t + \theta)$. The fundamental laser field $F_1 = 1.6$ V/nm. The second-harmonic ($\beta = 2$) laser field $F_2 = 0.22$ V/nm (experimental laser parameters in Ref. [27]). When $\theta = 0$, the normalized time-averaged emission current density $\langle w \rangle = 5.23 \times 10^{-10}$; when $\theta = \pi$, $\langle w \rangle = 7.31 \times 10^{-11}$.

of laser fields [24]. As the phase difference θ varies from 0 to π, $w(\bar{x}, t)$ becomes significantly smaller, due to the interference effect of the two lasers, which also causes the total time-averaged emission current density $\langle w \rangle$ to decrease

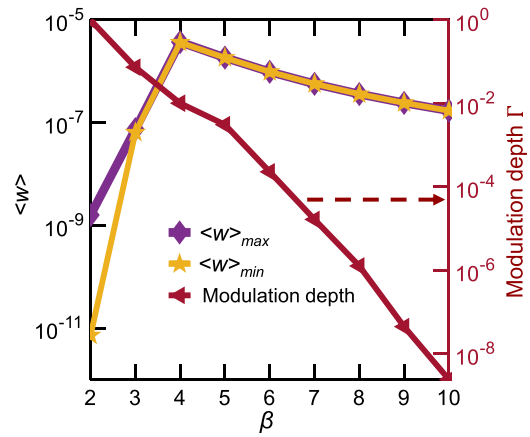

FIG. 6. Effects of the harmonic order. The emission current modulation depth Γ, the maximum and minimum time-averaged current density, $\langle w \rangle_{\max}$ and $\langle w \rangle_{\min}$, as a function of harmonic order β. The fundamental laser field F_1 and the harmonic laser field F_2 are 1.6 and 0.22 V/nm, respectively (intensity ratio of 2%).

from 5.23×10^{-10} to 7.31×10^{-11}. Figures 5(c) and 5(d) show the total emission current density $w(t)$ at $\bar{x} = 100$ as a function of time t. It is shown that $w(t)$ and the total laser field $F(t)$ have a clear phase shift, which means the peak value of time-dependent total emission current density does not occur at the peak value of the total incident laser field. As the phase difference θ changes, the temporal profile of the emission current density $w(\bar{x},\ t)$ for a fixed $\bar{x}$ also has a phase shift due to the interference effect between the two lasers. The full width at half maximum (FWHM) of the modulation of the ultrafast current pulses in Fig. 5 is approximately 0.62 fs, which is significantly shorter than the period of the fundamental laser period of 2.67 fs.

Figure 6 shows the effects of higher harmonic F_2 ($\beta > 2$) on the emission current modulation depth Γ. As β increases, Γ decreases, because of reduced interference between the two-color lasers [see Fig. 1(d)]. Note that superimposing the fourth-harmonic laser ($\beta = 4$) on the fundamental laser leads to the largest $\langle w \rangle_{\max}$ and $\langle w \rangle_{\min}$. This is in agreement with the prediction [24] that the maximum emission current occurs when the single-photon energy (i.e., the fourth-harmonic photon here) roughly equals the potential barrier, $4\hbar\omega / W \approx 1$.

IV. CONCLUSION

In summary, we have constructed an analytical model for ultrafast electron emission from a metal surface due to two-color lasers, by solving the time-dependent Schrödinger equation exactly. A single formulation captures various emission mechanisms, such as multiphoton absorption, photon-induced over-barrier emission, strong optical field emission, and various combinations of them. Our model demonstrates great tunability on the photoelectron spectrum, emission current, and current modulation depth, via the control of the phase delay, relative intensity, and harmonic order of the two-color lasers. We believe that such two-color induced photoemission can provide a promising way for ultrafast coherent control of electrons and may inspire a route towards designing of future ultrafast nanoelectronics.

Future research may consider the effects of band structure of the cathode material, electrode geometry and surface effects (e.g., local surface roughness, grain boundaries, different crystal terminations, etc.), space charge, dc bias, and short pulse illumination on two-color laser-induced electron emission. Image charge effects along with the Schottky barrier lowering due to additional dc bias will be studied. The effects of laser penetration depth and scattering effects of photoexcited electrons with phonons and other electrons will also be evaluated and compared with existing three-step models [20]. These studies could further facilitate the extension of our model to nonmetal cathodes (e.g., semiconductors and low-dimensional materials).

ACKNOWLEDGMENTS

We acknowledge useful discussions with Professors Y. Y. Lau, J. Luginsland, J. Verboncoeur, and S. Baryshev. The work is supported by the Air Force Office of Scientific Research (AFOSR) YIP Award No. FA9550-18-1-0061.

APPENDIX

Following Truscott [24,34], the time-dependent potential for $x \geqslant 0$ may be written as $\Phi(x,t) = V(x,t) - xf(t)$, with $V(x,t) = V_0$, and $f(t) = eF_1 \cos(\omega t) + eF_2 \cos(\beta\omega t + \theta)$. Thus, Eq. (2) in the text may be transformed to the coordinate system ξ, t, where $\xi = x - q(t)$, the displacement $q(t) = (1/m)\int^t p(t')dt'$, and $p(t) = \int^t f(t')dt'$, by assuming that $\psi(x,t) = \phi(\xi,t)\chi(x,t)$, with $\chi(x,t) = \exp[-iEt/\hbar + ixp(t)/\hbar - (i/2\hbar m)\int^t p^2(t')dt']$, with E being a constant. We have

$$i\hbar\frac{\partial\phi(\xi,t)}{\partial t} = \left[-\frac{\hbar^2}{2m}\frac{\partial^2}{\partial\xi^2} + U(\xi,t) - E\right]\phi(\xi,t), \quad \text{(A1)}$$

with $U(\xi,t) = V(x,t)$. By separation of variables, Eq. (A1) can be easily solved to give

$$\phi(\xi,t) = \phi(\xi) = e^{i\xi\sqrt{2m(E-V_0)/\hbar^2}}, \quad \text{(A2)}$$

From $\psi(x,t) = \phi(\xi)\chi(x,t)$, we obtain Eq. (3), which is the exact solution to Eq. (2), upon using $E = \varepsilon + n\hbar\omega - e^2F_1^2/4m\omega^2 - e^2F_2^2/4m\beta^2\omega^2$.

[1] P. Hommelhoff, C. Kealhofer, and M. A. Kasevich, Phys. Rev. Lett. **97**, 247402 (2006).
[2] R. Bormann, M. Gulde, A. Weismann, S. V. Yalunin, and C. Ropers, Phys. Rev. Lett. **105**, 147601 (2010).
[3] H. Yanagisawa, M. Hengsberger, D. Leuenberger, M. Klöckner, C. Hafner, T. Greber, and J. Osterwalder, Phys. Rev. Lett. **107**, 087601 (2011).
[4] G. Herink, D. R. Solli, M. Gulde, and C. Ropers, Nature **483**, 190 (2012).
[5] A. Mustonen, P. Beaud, E. Kirk, T. Feurer, and S. Tsujino, Appl. Phys. Lett. **99**, 103504 (2011).
[6] S. E. Irvine, A. Dechant, and A. Y. Elezzabi, Phys. Rev. Lett. **93**, 184801 (2004).
[7] S. Li and R. R. Jones, Nat. Commun. **7**, 13405 (2016).
[8] L. Wimmer, G. Herink, D. R. Solli, S. V. Yalunin, K. E. Echternkamp, and C. Ropers, Nat. Phys. **10**, 432 (2014).
[9] A. Feist, K. E. Echternkamp, J. Schauss, S. V. Yalunin, S. Schäfer, and C. Ropers, Nature **521**, 200 (2015).
[10] K. Yoshioka, I. Katayama, Y. Minami, M. Kitajima, S. Yoshida, H. Shigekawa, and J. Takeda, Nat. Photonics **10**, 762 (2016).
[11] M. Krüger, M. Schenk, and P. Hommelhoff, Nature **475**, 78 (2011).
[12] M. Kociak, Nature **521**, 166 (2015).
[13] C. Kealhofer, W. Schneider, D. Ehberger, A. Ryabov, F. Krausz, and P. Baum, Science **352**, 429 (2016).
[14] A. H. Zewail, Science **328**, 187 (2010).
[15] T. L. Cocker, D. Peller, P. Yu, J. Repp, and R. Huber, Nature **539**, 263 (2016).
[16] R. J. England, R. J. Noble, K. Bane, D. H. Dowell, C.-K. Ng, J. E. Spencer, S. Tantawi, Z. Wu, R. L. Byer, E. Peralta, K. Soong, C.-M. Chang, B. Montazeri, S. J. Wolf, B. Cowan, J. Dawson, W. Gai, P. Hommelhoff, Y.-C. Huang, C. Jing *et al.*, Rev. Mod. Phys. **86**, 1337 (2014).

[17] H. J. Caulfield and S. Dolev, Nat. Photonics **4**, 261 (2010).
[18] F. Krausz and M. I. Stockman, Nat. Photonics **8**, 205 (2014).
[19] P. Zhang, Á. Valfells, L. K. Ang, J. W. Luginsland, and Y. Y. Lau, Appl. Phys. Rev. **4**, 011304 (2017).
[20] J. P. Girardeau-Montaut and C. Girardeau-Montaut, Phys. Rev. B **51**, 13560 (1995).
[21] S. V. Yalunin, M. Gulde, and C. Ropers, Phys. Rev. B **84**, 195426 (2011).
[22] M. Pant and L. K. Ang, Phys. Rev. B **86**, 045423 (2012).
[23] M. Krüger, M. Schenk, P. Hommelhoff, G. Wachter, C. Lemell, and J. Burgdörfer, New J. Phys. **14**, 085019 (2012).
[24] P. Zhang and Y. Y. Lau, Sci. Rep. **6**, 19894 (2016).
[25] B. Piglosiewicz, S. Schmidt, D. J. Park, J. Vogelsang, P. Groß, C. Manzoni, P. Farinello, G. Cerullo, and C. Lienau, Nat. Photonics **8**, 37 (2014).
[26] D. J. Park, B. Piglosiewicz, S. Schmidt, H. Kollmann, M. Mascheck, and C. Lienau, Phys. Rev. Lett. **109**, 244803 (2012).
[27] M. Förster, T. Paschen, M. Krüger, C. Lemell, G. Wachter, F. Libisch, T. Madlener, J. Burgdörfer, and P. Hommelhoff, Phys. Rev. Lett. **117**, 217601 (2016).
[28] W. C.-W. Huang, M. Becker, J. Beck, and H. Batelaan, New J. Phys. **19**, 023011 (2017).
[29] P. Hommelhoff, Y. Sortais, A. Aghajani-Talesh, and M. A. Kasevich, Phys. Rev. Lett. **96**, 077401 (2006).
[30] J. W. Gadzuk and E. W. Plummer, Rev. Mod. Phys. **45**, 487 (1973).
[31] P. Zhang, Sci. Rep. **5**, 9826 (2015).
[32] H. Yanagisawa, C. Hafner, P. Doná, M. Klöckner, D. Leuenberger, T. Greber, J. Osterwalder, and M. Hengsberger, Phys. Rev. B **81**, 115429 (2010).
[33] A. Chatziafratis, G. Fikioris, and J. P. Xanthakis, Proc. R. Soc. A **474**, 20170692 (2018).
[34] W. S. Truscott, Phys. Rev. Lett. **70**, 1900 (1993).